

Low-distortion planar embedding of rod-based structures

Mark Yan Lok Yip^a, Gary P. T. Choi^{a,*}

^a*Department of Mathematics, The Chinese University of Hong Kong*

Abstract

Rod-based structures are commonly used in practical applications in science and engineering. However, in many design, analysis, and manufacturing tasks, handling the rod-based structures in three dimensions directly is generally challenging. To simplify the tasks, it is usually more desirable to achieve a two-dimensional representation of the rod-based structures via some suitable geometric mappings. In this work, we develop a novel method for computing a low-distortion planar embedding of rod-based structures. Specifically, we identify geometrical constraints that aim to preserve key length and angle quantities of the 3D rod-based structures and prevent the occurrence of overlapping rods in the planar embedding. Experimental results with a variety of rod-based structures are presented to demonstrate the effectiveness of our approach. Moreover, our method can be naturally extended to the design and mapping of hybrid structures consisting of both rods and surface elements. Altogether, our approach paves a new way for the efficient design and fabrication of novel three-dimensional geometric structures for practical applications.

*Corresponding author.

Keywords: rod-based structures, planar embedding, geometric mapping, constrained optimization, computational fabrication

1. Introduction

The design and analysis of geometric structures are important in many applications in science and engineering. In recent years, there has been an increasing interest in the use of wireframe or gridshell structures. For instance, structures consisting of strip elements can be utilized in the design of complex shapes in architecture [1]. Structures consisting of rod-like elements are also commonly found in 3D or 4D printing [2]. The high flexibility in such structures also makes them very suitable for achieving different shape transformation effects [3, 4]. Therefore, many recent approaches have focused on the design of different rod-based and gridshell structures, such as the elastic and thermoelastic materials [5], elastic gridshells [6, 7], self-actuated shells for morphing into a prescribed 3D shape [8], surface discretization using strips [9], surface-based inflatables [10, 11], and hybrid gridshell structures [12].

While these 3D rod-based and gridshell structures are highly flexible and widely applicable to different problems, the design and analysis of them require the consideration of various geometric aspects. Also, from the perspective of fabrication, storage, and transportation, directly handling the 3D structures may be inefficient. To simplify the process, one possible approach is to flatten the 3D structures and embed them on a planar domain. More specifically, the 2D representation of the structures will not only allow for easier design and comparison but also facilitate the practical manufacturing of the structures. However, to ensure that the 2D representation can accurately represent the

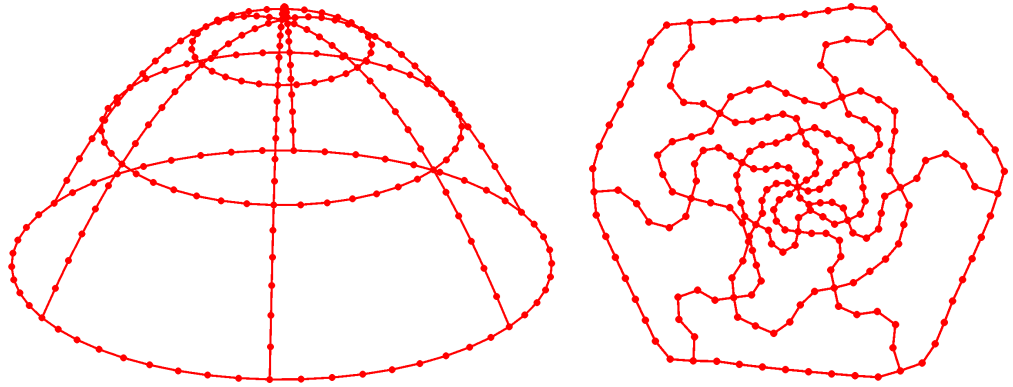


Figure 1: **An illustration of the proposed low-distortion planar embedding method for 3D rod-based structures in our work.** Given a 3D rod-based structure with a prescribed target shape (left), our proposed method aims to produce a planar configuration of the structure that possesses low geometric distortion (right) with key rod length and angle quantities preserved, thereby facilitating the modelling and manufacturing of the rod-based structures for practical applications.

original 3D rod-based structures, it is important to preserve certain key geometric properties of the 3D structures and minimize the overall geometric distortion of the embedding.

In this work, we develop a novel method for achieving a low-distortion planar embedding of rod-based structures (Fig. 1). More specifically, our proposed method takes an arbitrary 3D rod-based structure consisting of vertices and short rod segments as input and produces a planar representation of it with minimal geometric distortion, preserving the lengths of the short rod segments and key intersection angles between rods. The method also automatically detects and corrects overlaps between rod segments to ensure a one-to-one correspondence between the planar representation and the original 3D structure. Experimental results on a large variety of rod-based structures are presented to demonstrate the effectiveness of our proposed method. We

further extend the method for handling more complex hybrid structures and consider the 2D-to-3D morphing process to showcase the flexibility and applicability of our method.

The rest of the paper is organized as follows. In Section 2, we describe the formulation and algorithm of our proposed low-distortion planar embedding method, including the details of the optimization problem we consider and the corresponding objective and constraint functions. In Section 3, we test our proposed method on a large variety of rod-based structures with different geometric properties to demonstrate its effectiveness. In Section 4, we further extend our computational framework for hybrid structures consisting of not only one-dimensional rods but also some surface regions. In Section 5, we simulate the 2D-to-3D morphing process of our planar embedding results to verify their practicability in real-world applications. We conclude the paper and discuss future directions in Section 6.

2. Proposed method

Let $\mathcal{S} = (\mathcal{V}, \mathcal{E})$ be a 3D rod-based structure, where \mathcal{V} is the vertex set with m vertices in it and \mathcal{E} is the edge set with p edges in it. Each vertex $v_i = (x_i, y_i, z_i) \in \mathcal{V}$ is a node in \mathbb{R}^3 , and each (undirected) edge $e_{ij} = [v_i, v_j] \in \mathcal{E}$ represents a short rod segment connecting node v_i and node v_j . Our goal is to obtain a low-distortion planar embedding $f : \mathcal{S} \rightarrow \mathbb{R}^m \times \mathbb{R}^m$ that preserves the key geometric features of \mathcal{S} as much as possible. The set $\mathcal{P} = f(\mathcal{S})$ will exactly be the vertex set of the planar embedding, and hence $(\mathcal{P}, \mathcal{E})$ will be the desired 2D representation of the rod-based structure.

2.1. Initial embedding

The first step of our proposed method is to construct an initial embedding $f_0 : \mathcal{S} \rightarrow \mathbb{R}^m \times \mathbb{R}^m$ of the given 3D rod-based structure. With the initial embedding, the subsequent computations can then be handled as a 2D-to-2D optimization problem more easily, as we can fix the dimension of the structure in \mathbb{R}^2 during the optimization process.

To achieve this initial embedding, one possible approach is to compute a Tutte embedding [13]. More specifically, we solve the following equation

$$L\mathbf{v} = 0, \quad (1)$$

where \mathbf{v} are the desired 2D coordinates of the vertices in the initial embedding and L is a $m \times m$ matrix known as the graph Laplacian:

$$L_{ij} = \begin{cases} 1, & \text{if } [v_i, v_j] \in \mathcal{E}, \\ -\sum_{k=1, k \neq i}^m L_{ik}, & \text{if } i = j, \\ 0, & \text{otherwise,} \end{cases} \quad (2)$$

subject to some prescribed constraints $f_0(v_{\text{bdy}_i}) = w_i$ for all outermost vertices $v_{\text{bdy}_1}, v_{\text{bdy}_2}, \dots, v_{\text{bdy}_k}$, with w_i being some prescribed position for the vertex v_{bdy_i} for this initial step. By solving the above-mentioned equation, we can obtain a set of vertex coordinates $\mathcal{P}_0 = f_0(\mathcal{S})$ on the plane, which serves as our initialization.

We remark that besides the Tutte embedding method, one may also consider other methods for efficiently obtaining the initial embedding. For instance, for some rod-based structures with relatively simple geometry, one

may directly compute a projection $(x, y, z) \rightarrow (x, y)$ for the initial embedding. It may also be possible to combine some mesh flattening methods with other planar transformations to construct the initial embedding.

2.2. Shape optimization

Once we have obtained the initial embedding $f_0 : \mathcal{S} \rightarrow \mathcal{P}_0$, we focus on solving a planar shape optimization problem and search for an optimized planar mapping $g : \mathcal{P}_0 \rightarrow \mathcal{P}$ that satisfies certain geometrical constraints. Below, we describe the geometrical constraints and their formulations in detail. Also, to enhance the computational efficiency and accuracy of the optimization process, we further derive the explicit formulas of the Jacobian of all constraints and objective functions.

First, note that to achieve a meaningful and accurate planar representation of the 3D rod-based structures, it is natural to consider the distortion of the rod segments and their joints. Specifically, it is desired that the planar shape in the optimized form should preserve the rod segment lengths and the angles at the joints of rods. Also, there should be no overlaps between the rods in the planar representation. This motivates us to consider three major constraints, namely (i) the *length-preserving constraints*, (ii) the *angle-preserving constraints*, and (iii) the *no-overlap constraints*.

2.2.1. Length-preserving constraints

Specifically, for the length-preserving constraints, we aim to enforce the preservation of the length for all rod segments in the planar embedding. To achieve this, let $l_i = \|v_{e_i(1)} - v_{e_i(2)}\|$ to be the length of each rod segment $e_i = [e_i(1), e_i(2)]$ in the 3D rod-based structure $(\mathcal{V}, \mathcal{E})$, and let $L_i = \|p_{e_i(1)} - p_{e_i(2)}\|$

be the length of the corresponding rod segment in the planar embedding $(\mathcal{P}, \mathcal{E})$. Here, $\|\cdot\|$ is defined to be the Euclidean norm. To preserve the length, it is desired to have $l_i = L_i$. From a computational perspective, since different rods in the overall rod-based structures may have different lengths, to ensure a fair consideration of all rods, we have the following length-preserving constraint:

$$E_L(e_i) = \frac{L_i}{l_i} - 1 = 0. \quad (3)$$

It is easy to see that $E_L(e_i) = 0$ if and only if $L_i = l_i$. Also, note that E_L is dimensionless.

Now, we further derive the gradient of this constraint by differentiating it with respect to the vertices in the planar embedding \mathcal{P} . For each i , note that l_i is given by the original 3D rod-based structure and can be treated as a constant. Let $p_{e_i(1)} = (x_{i_1}, y_{i_1})$ and $p_{e_i(2)} = (x_{i_2}, y_{i_2})$. We have

$$E_L(e_i) = \frac{\sqrt{(x_{i_1} - x_{i_2})^2 + (y_{i_1} - y_{i_2})^2}}{l_i} - 1. \quad (4)$$

Using the chain rule, we have

$$\frac{\partial E_L(e_i)}{\partial x_{i_1}} = \frac{2(x_{i_1} - x_{i_2})}{2\sqrt{(x_{i_1} - x_{i_2})^2 + (y_{i_1} - y_{i_2})^2} \cdot l_i} = \frac{x_{i_1} - x_{i_2}}{L_i \cdot l_i}. \quad (5)$$

Similarly, we have

$$\frac{\partial E_L(e_i)}{\partial y_{i_1}} = \frac{y_{i_1} - y_{i_2}}{L_i \cdot l_i}, \quad \frac{\partial E_L(e_i)}{\partial x_{i_2}} = \frac{-(x_{i_1} - x_{i_2})}{L_i \cdot l_i}, \quad \frac{\partial E_L(e_i)}{\partial y_{i_2}} = \frac{-(y_{i_1} - y_{i_2})}{L_i \cdot l_i}. \quad (6)$$

Thus, if we consider all variables as $(x_1, x_2, \dots, x_m, y_1, y_2, \dots, y_m)$, where m

is the total number of vertices, we have

$$\nabla E_L(e_i) = \left[0 \ \dots \ 0 \ \frac{\partial E_L(e_i)}{\partial x_{i_1}} \ 0 \ \dots \ \frac{\partial E_L(e_i)}{\partial x_{i_1}} \ 0 \ \dots \ \frac{\partial E_L(e_i)}{\partial x_{i_1}} \ 0 \ \dots \ \frac{\partial E_L(e_i)}{\partial x_{i_1}} \ \dots \ 0 \right]^T. \quad (7)$$

In other words, for each i , there are exactly four non-zero entries in $\nabla E_L(e_i)$.

2.2.2. Angle-preserving constraints

Next, for the angle-preserving constraints, we aim to preserve the angles at the joints of the rods. Here, the joints of the rods are the special location at which two chains of rods (each representing a curve) meet, instead of every intersection point between two adjacent rods. This ensures that the overall directions of the rod chains are largely preserved in the planar representation. From a more practical perspective, since such joints are generally the more fragile part of the rod-based structures, preserving the angles at those joints would be beneficial for reducing the distortion induced locally at them during shape morphing or deformations.

First, we denote all angles at the joints in both the original 3D rod-based structure and the 2D planar embedding as $\{\theta_{3D_j}\}_{j=1}^q$ and $\{\theta_{2D_j}\}_{j=1}^q$, where q is the total number of angles, and every pair of angles $(\theta_{3D_j}, \theta_{2D_j})$ are the angles formed the corresponding vertices in 3D and 2D. The angles can be easily expressed in terms of the vertex coordinates as detailed in [14]. Then, for every $j = 1, 2, \dots, q$, we consider the angle-preserving constraint

$$E_A(j) = \cos(\theta_{2D_j}) - \cos(\theta_{3D_j}) = 0. \quad (8)$$

Here, we use $\cos(\theta_{2D_j}), \cos(\theta_{3D_j})$ instead of $\theta_{2D_j}, \theta_{3D_j}$ so that the gradient of

$E_A(j)$ can be expressed in terms of vertex coordinates more easily. Specifically, note that θ_{3D_j} is given by the original 3D rod-based structure and hence $\cos(\theta_{3D_j})$ can be treated as a constant. Now, for each angle θ_{2D_j} , we look up the three corresponding vertices in the planar embedding. Denote them as $p_{\theta_j(1)} = (x_{j_1}, y_{j_1})$, $p_{\theta_j(2)} = (x_{j_2}, y_{j_2})$, and $p_{\theta_j(3)} = (x_{j_3}, y_{j_3})$. We further let

$$\vec{a} = \begin{bmatrix} x_{j_2} \\ y_{j_2} \end{bmatrix} - \begin{bmatrix} x_{j_1} \\ y_{j_1} \end{bmatrix} \quad \text{and} \quad \vec{b} = \begin{bmatrix} x_{j_3} \\ y_{j_3} \end{bmatrix} - \begin{bmatrix} x_{j_1} \\ y_{j_1} \end{bmatrix}. \quad (9)$$

Then, we have

$$\cos(\theta_{2D}) = \frac{\vec{a} \cdot \vec{b}}{\|\vec{a}\| \|\vec{b}\|}. \quad (10)$$

By writing $c = \vec{a} \cdot \vec{b}$, we can take partial derivatives of c with respect to x_{j_1} and y_{j_1} :

$$\frac{\partial c}{\partial x_{j_1}} = 2x_{j_1} - x_{j_2} - x_{j_3}, \quad \frac{\partial c}{\partial y_{j_1}} = 2y_{j_1} - y_{j_2} - y_{j_3}. \quad (11)$$

Similarly, we can take partial derivatives of c with respect to x_{j_2} , y_{j_2} , x_{j_3} , y_{j_3} and get:

$$\frac{\partial c}{\partial x_{j_2}} = x_{j_3} - x_{j_1}, \quad \frac{\partial c}{\partial y_{j_2}} = y_{j_3} - y_{j_1}, \quad \frac{\partial c}{\partial x_{j_3}} = x_{j_2} - x_{j_1}, \quad \frac{\partial c}{\partial y_{j_3}} = y_{j_2} - y_{j_1}. \quad (12)$$

Next, we take the partial derivatives of $\|\vec{a}\|$ with respect to x_{j_1} , y_{j_1} :

$$\frac{\partial \|\vec{a}\|}{\partial x_{j_1}} = \frac{x_{j_1} - x_{j_2}}{\|\vec{a}\|}, \quad \frac{\partial \|\vec{a}\|}{\partial y_{j_1}} = \frac{y_{j_1} - y_{j_2}}{\|\vec{a}\|}, \quad (13)$$

Similarly, for x_{j_2}, y_{j_2} , we have

$$\frac{\partial||\vec{a}||}{\partial x_{j_2}} = \frac{x_{j_2} - x_{j_1}}{||\vec{a}||}, \quad \frac{\partial||\vec{a}||}{\partial y_{j_2}} = \frac{y_{j_2} - y_{j_1}}{||\vec{a}||}. \quad (14)$$

Since \vec{a} does not involve x_{j_3}, y_{j_3} , it is easy to see that

$$\frac{\partial||\vec{a}||}{\partial x_{j_3}} = \frac{\partial||\vec{a}||}{\partial y_{j_3}} = 0. \quad (15)$$

Analogously, for $||\vec{b}||$, we have:

$$\frac{\partial||\vec{b}||}{\partial x_{j_1}} = \frac{x_{j_1} - x_{j_3}}{||\vec{b}||}, \quad \frac{\partial||\vec{b}||}{\partial y_{j_1}} = \frac{y_{j_1} - y_{j_3}}{||\vec{b}||}, \quad (16)$$

$$\frac{\partial||\vec{b}||}{\partial x_{j_2}} = \frac{\partial||\vec{b}||}{\partial y_{j_2}} = 0, \quad (17)$$

$$\frac{\partial||\vec{b}||}{\partial x_{j_3}} = \frac{x_{j_3} - x_{j_1}}{||\vec{b}||}, \quad \frac{\partial||\vec{b}||}{\partial y_{j_3}} = \frac{y_{j_3} - y_{j_1}}{||\vec{b}||}. \quad (18)$$

Thus, for $k = 1, 2, 3$, the partial derivative of the angle constraint $E_A(j)$ with respect to all x_{j_k}, y_{j_k} are:

$$\frac{\partial E_A(j)}{\partial x_{j_k}} = \frac{\frac{\partial c}{\partial x_{j_k}}||\vec{a}||||\vec{b}|| - (\vec{a} \cdot \vec{b})(\frac{\partial||\vec{a}||}{\partial x_{j_k}}||\vec{b}|| + \frac{\partial||\vec{b}||}{\partial x_{j_k}}||\vec{a}||)}{||\vec{a}||^2||\vec{b}||^2} \quad (19)$$

and

$$\frac{\partial E_A(j)}{\partial y_{j_k}} = \frac{\frac{\partial c}{\partial y_{j_k}}||\vec{a}||||\vec{b}|| - (\vec{a} \cdot \vec{b})(\frac{\partial||\vec{a}||}{\partial y_{j_k}}||\vec{b}|| + \frac{\partial||\vec{b}||}{\partial y_{j_k}}||\vec{a}||)}{||\vec{a}||^2||\vec{b}||^2}, \quad (20)$$

in which all the intermediate partial derivative terms have already been derived above.

Thus, if we consider all variables as $(x_1, x_2, \dots, x_m, y_1, y_2, \dots, y_m)$, we have

$$\nabla E_A(j) = \begin{bmatrix} 0 & \dots & \frac{\partial E_A(j)}{\partial x_{j_1}} & \dots & \frac{\partial E_A(j)}{\partial x_{j_2}} & \dots & \frac{\partial E_A(j)}{\partial x_{j_3}} & \dots & \frac{\partial E_A(j)}{\partial y_{j_1}} & \dots & \frac{\partial E_A(j)}{\partial y_{j_2}} & \dots & \frac{\partial E_A(j)}{\partial y_{j_3}} & \dots & 0 \end{bmatrix}^T. \quad (21)$$

In other words, for each j , there are exactly six non-zero entries in $\nabla E_A(j)$.

2.2.3. No-overlap constraints

As discussed previously, the third type of constraints in our formulation is the no-overlap constraints, which aim to prevent the overlap between rod segments in the planar embedding result. While the most direct way is to consider all pairs of rod segments and check all possible occurrences of overlaps, the large number of combinations is computationally expensive. Moreover, designing a suitable constraint function for preventing such occurrences is highly nontrivial. Therefore, instead of directly working with the overlaps, we propose an alternative implicit formulation for the no-overlap constraints.

More specifically, denote $\tilde{\mathcal{B}}$ as the collection of all boundary vertices of the initial planar embedding. We first consider building a triangulation $\{\tilde{T}_1, \tilde{T}_2, \dots, \tilde{T}_n\}$ on the initial planar embedding result so that the sum of all triangle areas is equal to the area enclosed by the vertices in $\tilde{\mathcal{B}}$, i.e.,

$$\sum_{i=1}^n \text{Area}(\tilde{T}_i) = \text{Area}(\tilde{\mathcal{B}}). \quad (22)$$

Now, to enforce that there is no overlap in the shape optimization result, we

consider the following no-overlap constraint:

$$E_O = \sum_{i=1}^n \text{Area}(T_i) - \text{Area}(\mathcal{B}) = 0, \quad (23)$$

where T_i represents the i -th triangle with the updated positions $p_{T_i(1)} = (x_{i1}, y_{i1})$, $p_{T_i(2)} = (x_{i2}, y_{i2})$ and $p_{T_i(3)} = (x_{i3}, y_{i3})$ induced by the above triangulation, and \mathcal{B} represents the updated coordinates of the vertices on the boundary induced by $\tilde{\mathcal{B}}$. To justify this formulation, we establish the following result:

Theorem 1. *If the area enclosed by all boundary vertices in the shape optimization result is equal to the area sum of all triangles, then there is no overlap in the shape optimization result.*

Proof. By assumption, we have $\sum_{i=1}^n \text{Area}(T_i) = \text{Area}(\mathcal{B})$ for the shape optimization result.

Now, suppose there is still at least one overlap in the shape optimization result. Then, there exist two triangles T_k and T_j such that $T_k \cap T_j \neq \emptyset$. Let $\mathcal{O} = T_k \cap T_j$. Since \mathcal{O} is non-empty, we have $\text{Area}(\mathcal{O}) > 0$.

In the summation $\sum_{i=1}^n \text{Area}(T_i)$, $\text{Area}(\mathcal{O})$ is counted in both $\text{Area}(T_k)$ and $\text{Area}(T_j)$. Therefore,

$$\text{Area}(\mathcal{B}) = \sum_{i=1}^n \text{Area}(T_i) = \text{Area}(\mathcal{O}) + \text{Area}(\mathcal{B}) > \text{Area}(\mathcal{B}), \quad (24)$$

which leads to a contradiction. Therefore, the shape optimization result will not have any overlaps if $\sum_{i=1}^n \text{Area}(T_i) = \text{Area}(\mathcal{B})$. ■

From the above result, we see that enforcing Eq. (23) will effectively

prevent the occurrence of overlaps throughout the shape optimization process. However, we remark that the other direction of the statement does not hold. In Fig. 2, we show a simple counterexample. In particular, Fig. 2(a) shows an example of the initial embedding of a rod-based structure and the Delaunay triangulation constructed based on all its vertices. In Fig. 2(b), we show a deformed configuration of the planar embedding. It is noteworthy that the deformed rod-based structure does not contain any rod overlaps. However, several overlaps can be found in the underlying triangulation under the deformation, indicating that the area enclosed by all boundary vertices in the deformed triangulation is not equal to the sum of all individual triangle areas. This example shows that the other direction of the theorem does not necessarily hold. In other words, while the condition can fulfill our needs for preventing overlaps between rods, it may be too strict in some cases and overconstrains our problem. In a later section, we will discuss how we can address this aspect by introducing an alternating minimization procedure in our overall proposed algorithm.

Now, we further derive the gradient of the constraint E_O in Eq. (23) as follows. First, we express $E_O = H - S$ in terms of the vertices in \mathcal{P} , where H represents the triangle area sum term and S represents the boundary area term. We handle the two terms one by one. First, for each triangle T_i , we can let $p_{T_i(1)} = (x_{i_1}, y_{i_1})$, $p_{T_i(2)} = (x_{i_2}, y_{i_2})$ and $p_{T_i(3)} = (x_{i_3}, y_{i_3})$. If we denote the three edges of T_i as L_{12_i} , L_{23_i} , L_{31_i} , we have

$$L_{12_i} = \sqrt{(x_{i_1} - x_{i_2})^2 + (y_{i_1} - y_{i_2})^2}, \quad (25)$$

$$L_{23_i} = \sqrt{(x_{i_2} - x_{i_3})^2 + (y_{i_2} - y_{i_3})^2}, \quad (26)$$

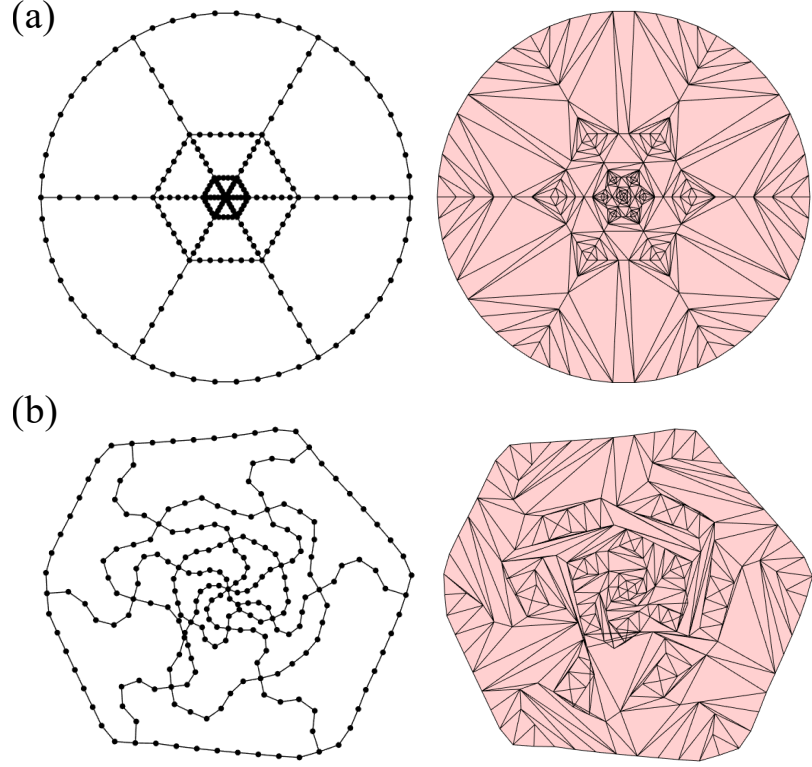


Figure 2: **An illustration of the construction of triangulations for the no-overlap constraint.** (a) An initial embedding of a rod-based structure and a Delaunay triangulation constructed on the set of all nodes. (b) An example of a deformed configuration of the planar embedding, with the associated triangulation induced from (a). It can be observed that the deformed rod-based structure does not contain overlaps, while several mesh overlaps can be found in the induced deformed triangulation, suggesting that the no-overlap constraint in Eq. (23) is sufficient but not necessary for ensuring the no-overlap condition.

$$L_{31_i} = \sqrt{(x_{i_3} - x_{i_1})^2 + (y_{i_3} - y_{i_1})^2}. \quad (27)$$

Therefore, using the Heron's formula, the triangle area sum is given by

$$H = \sum_{i=1}^n \sqrt{s_i(s_i - L_{12_i})(s_i - L_{23_i})(s_i - L_{31_i})}, \quad (28)$$

where

$$s_i = \frac{L_{12i} + L_{23i} + L_{31i}}{2} \quad (29)$$

for all $i = 1, 2, \dots, n$.

As for the boundary area term, if we denote the indices of the boundary vertices as b_1, b_2, \dots, b_s , using the shoelace formula, the boundary area is given by

$$\begin{aligned} S &= \frac{1}{2} \begin{vmatrix} x_{b_1} & x_{b_2} & x_{b_3} & \cdots & x_{b_s} & x_{b_1} \\ y_{b_1} & y_{b_2} & y_{b_3} & \cdots & y_{b_s} & y_{b_1} \end{vmatrix} \\ &= \frac{1}{2} (x_{b_1}y_{b_2} + x_{b_2}y_{b_3} + \cdots + x_{b_s}y_{b_1} - x_{b_2}y_{b_1} - x_{b_3}y_{b_2} + \cdots - x_{b_1}y_{b_s}). \end{aligned} \quad (30)$$

From Eq. (28) and Eq. (30), we see that E_O can be expressed explicitly in terms of the vertices in \mathcal{P} .

To get the gradient of E_O , we have to differentiate it with respect to the whole \mathcal{P} . For the triangulation part H , note that each T_i only involves the vertex coordinates $x_{i_1}, x_{i_2}, x_{i_3}$ and $y_{i_1}, y_{i_2}, y_{i_3}$, and hence the derivative of the area term for T_i with respect to all other variables can be omitted. Below, for convenience, we write $x_{i_1} = x_1$ and similarly for x_2, x_3, y_1, y_2, y_3 to illustrate the derivation once. For $\alpha, \beta, \gamma = 1, 2, 3$, where $\alpha \neq \beta \neq \gamma$, we can easily get

$$\frac{\partial L_{\alpha\beta}}{\partial x_\alpha} = \frac{x_\alpha - x_\beta}{L_{\alpha\beta}}, \quad \frac{\partial L_{\alpha\beta}}{\partial y_\alpha} = \frac{y_\alpha - y_\beta}{L_{\alpha\beta}}, \quad (31)$$

$$\frac{\partial L_{\alpha\beta}}{\partial x_\beta} = \frac{-(x_\alpha - x_\beta)}{L_{\alpha\beta}}, \quad \frac{\partial L_{\alpha\beta}}{\partial y_\beta} = \frac{-(y_\alpha - y_\beta)}{L_{\alpha\beta}}, \quad (32)$$

$$\frac{\partial L_{\alpha\beta}}{\partial x_\gamma} = \frac{\partial L_{\alpha\beta}}{\partial y_\gamma} = 0. \quad (33)$$

Then, for $m = 1, 2, 3$, we have

$$\begin{aligned} \frac{\partial \text{Area}(T_i)}{\partial x_m} = & \\ \frac{4L_{12}(L_{23}^2 + L_{31}^2 - L_{12}^2)\frac{\partial L_{12}}{\partial x_k} + 4L_{23}(L_{31}^2 + L_{12}^2 - L_{23}^2)\frac{\partial L_{23}}{\partial x_k} + 4L_{31}(L_{12}^2 + L_{23}^2 - L_{31}^2)\frac{\partial L_{31}}{\partial x_k}}{8\sqrt{(L_{12} + L_{23} + L_{31})(L_{12} + L_{23} - L_{31})(L_{12} - L_{23} + L_{31})(-L_{12} + L_{23} + L_{31})}} \end{aligned} \quad (34)$$

and

$$\begin{aligned} \frac{\partial \text{Area}(T_i)}{\partial y_m} = & \\ \frac{4L_{12}(L_{23}^2 + L_{31}^2 - L_{12}^2)\frac{\partial L_{12}}{\partial y_k} + 4L_{23}(L_{31}^2 + L_{12}^2 - L_{23}^2)\frac{\partial L_{23}}{\partial y_k} + 4L_{31}(L_{12}^2 + L_{23}^2 - L_{31}^2)\frac{\partial L_{31}}{\partial y_k}}{8\sqrt{(L_{12} + L_{23} + L_{31})(L_{12} + L_{23} - L_{31})(L_{12} - L_{23} + L_{31})(-L_{12} + L_{23} + L_{31})}}. \end{aligned} \quad (35)$$

Hence, for each $k = 1, 2, 3, \dots, m$, we simply need to add up the partial derivatives of all individual triangle area terms. We have:

$$\frac{\partial H}{\partial x_k} = \sum_{i=1}^n \frac{\partial \text{Area}(T_i)}{\partial x_k} \quad \text{and} \quad \frac{\partial H}{\partial y_k} = \sum_{i=1}^n \frac{\partial \text{Area}(T_i)}{\partial y_k}. \quad (36)$$

This shows how the partial derivatives of H with respect to each vertex coordinate can be derived.

For the boundary area term S , it suffices to differentiate it with respect to the coordinates of all boundary vertices \mathcal{B} , i.e., $x_{b_1}, x_{b_2}, x_{b_3}, \dots, x_{b_s}$ and $y_{b_1}, y_{b_2}, y_{b_3}, \dots, y_{b_s}$. For $k = 1, \dots, s$, from Eq. (30) we can easily get

$$\frac{\partial S}{\partial x_{b_k}} = \frac{y_{b_{(k+1)}} - y_{b_{(s+1-k)}}}{2} \quad \text{and} \quad \frac{\partial S}{\partial y_{b_k}} = \frac{x_{b_{(s+1-k)}} - x_{b_{(k+1)}}}{2}. \quad (37)$$

For all other vertices $p_k \in \mathcal{P} \setminus \mathcal{B}$, we have $\frac{\partial S}{\partial x_k} = \frac{\partial S}{\partial y_k} = 0$.

Putting the above results together, the gradient of the no-overlap constraint

is given by

$$\nabla E_O = \begin{bmatrix} \partial_{x_1} H - \partial_{x_1} S \\ \partial_{x_2} H - \partial_{x_2} S \\ \partial_{x_3} H - \partial_{x_3} S \\ \vdots \\ \partial_{x_m} H - \partial_{x_m} S \\ \partial_{y_1} H - \partial_{y_1} S \\ \partial_{y_2} H - \partial_{y_2} S \\ \partial_{y_3} H - \partial_{y_3} S \\ \vdots \\ \partial_{y_m} H - \partial_{y_m} S \end{bmatrix}. \quad (38)$$

2.2.4. The objective function and the constrained optimization formulation

After describing all constraints to be satisfied, we move on to the design of the objective function in our shape optimization problem. Note that in the constraints, we have primarily focused on the length of each individual rod segment and the angles at specific joints. To further achieve a low overall geometric distortion of the structure, we may consider the remaining angle quantities in the structure that we have not yet covered, i.e., the angles between adjacent individual rod segments. It is easy to see that if the values of these angles in the planar embedding are largely similar to those in the 3D structure, then it implies that there are fewer unnatural bends or sharp orientation changes among neighboring rods, and hence the overall geometric distortion of the embedding should be small.

Motivated by the above, we consider the following angle-based objective

function:

$$E = \sum_{i=1}^r (\cos(\phi_{2D_i}) - \cos(\phi_{3D_i}))^2, \quad (39)$$

where r is the total number of angles between adjacent rod segments, ϕ_{2D_i} is the angle value in the planar embedding, and ϕ_{3D_i} is the corresponding angle value in the original 3D structure. To simplify our discussion below, we further denote

$$E_i = (\cos(\phi_{2D_i}) - \cos(\phi_{3D_i}))^2. \quad (40)$$

Analogous to the discussion of the angle-preserving constraint in Eq. (8), here note that we can express E and its gradient in terms of the 2D vertex coordinates. Again, all ϕ_{3D_i} values are given by the original 3D structure and hence $\cos(\phi_{3D_i})$ can be treated as a constraint. For the term $\cos(\phi_{2D_i})$, note that each angle involves three vertices and we denote them as $p_{\phi_{2D_i}(1)} = (x_1, y_1)$, $p_{\phi_{2D_i}(2)} = (x_2, y_2)$, $p_{\phi_{2D_i}(3)} = (x_3, y_3)$. Then we have

$$\vec{a} = \begin{bmatrix} x_2 \\ y_2 \end{bmatrix} - \begin{bmatrix} x_1 \\ y_1 \end{bmatrix}, \quad \vec{b} = \begin{bmatrix} x_3 \\ y_3 \end{bmatrix} - \begin{bmatrix} x_1 \\ y_1 \end{bmatrix}, \quad \cos(\phi_{2D_i}) = \frac{\vec{a} \cdot \vec{b}}{\|\vec{a}\| \|\vec{b}\|}. \quad (41)$$

Letting $c = \vec{a} \cdot \vec{b}$, we get

$$\frac{\partial c}{\partial x_1} = 2x_1 - x_2 - x_3, \quad \frac{\partial c}{\partial y_1} = 2y_1 - y_2 - y_3, \quad (42)$$

$$\frac{\partial c}{\partial x_2} = x_3 - x_1, \quad \frac{\partial c}{\partial y_2} = y_3 - y_1, \quad (43)$$

$$\frac{\partial c}{\partial x_3} = x_2 - x_1, \quad \frac{\partial c}{\partial y_3} = y_2 - y_1. \quad (44)$$

Also,

$$\frac{\partial \|\vec{a}\|}{\partial x_1} = \frac{x_1 - x_2}{\|\vec{a}\|}, \quad \frac{\partial \|\vec{a}\|}{\partial y_1} = \frac{y_1 - y_2}{\|\vec{a}\|}, \quad (45)$$

$$\frac{\partial \|\vec{a}\|}{\partial x_2} = \frac{x_2 - x_1}{\|\vec{a}\|}, \quad \frac{\partial \|\vec{a}\|}{\partial y_2} = \frac{y_2 - y_1}{\|\vec{a}\|}, \quad (46)$$

$$\frac{\partial \|\vec{a}\|}{\partial x_3} = \frac{\partial \|\vec{a}\|}{\partial y_3} = 0, \quad (47)$$

and

$$\frac{\partial \|\vec{b}\|}{\partial x_1} = \frac{x_1 - x_3}{\|\vec{b}\|}, \quad \frac{\partial \|\vec{b}\|}{\partial y_1} = \frac{y_1 - y_3}{\|\vec{b}\|}, \quad (48)$$

$$\frac{\partial \|\vec{b}\|}{\partial x_2} = \frac{\partial \|\vec{b}\|}{\partial y_2} = 0, \quad (49)$$

$$\frac{\partial \|\vec{b}\|}{\partial x_3} = \frac{x_3 - x_1}{\|\vec{b}\|}, \quad \frac{\partial \|\vec{b}\|}{\partial y_3} = \frac{y_3 - y_1}{\|\vec{b}\|}. \quad (50)$$

From the above, for each term E_i and $k = 1, 2, 3$, we have

$$\frac{\partial E_i}{\partial x_k} = \frac{2 \left(\frac{\vec{a} \cdot \vec{b}}{\|\vec{a}\| \|\vec{b}\|} - \cos(\phi_{3D_i}) \right) \left[\frac{\partial c}{\partial x_k} \|\vec{a}\| \|\vec{b}\| - (\vec{a} \cdot \vec{b}) \left(\frac{\partial \|\vec{a}\|}{\partial x_k} \|\vec{b}\| + \frac{\partial \|\vec{b}\|}{\partial x_k} \|\vec{a}\| \right) \right]}{\|\vec{a}\|^2 \|\vec{b}\|^2}, \quad (51)$$

$$\frac{\partial E_i}{\partial y_k} = \frac{2 \left(\frac{\vec{a} \cdot \vec{b}}{\|\vec{a}\| \|\vec{b}\|} - \cos(\phi_{3D_i}) \right) \left[\frac{\partial c}{\partial y_k} \|\vec{a}\| \|\vec{b}\| - (\vec{a} \cdot \vec{b}) \left(\frac{\partial \|\vec{a}\|}{\partial y_k} \|\vec{b}\| + \frac{\partial \|\vec{b}\|}{\partial y_k} \|\vec{a}\| \right) \right]}{\|\vec{a}\|^2 \|\vec{b}\|^2}. \quad (52)$$

Therefore, for each $p_k = (x_k, y_k) \in \mathcal{P}$, where $k = 1, 2, 3, \dots, m$, we have

$$\frac{\partial E}{\partial x_k} = \sum_{i=1}^r \frac{\partial E_i}{\partial x_k} \quad \text{and} \quad \frac{\partial E}{\partial y_k} = \sum_{i=1}^r \frac{\partial E_i}{\partial y_k}. \quad (53)$$

Hence, the gradient of the objective function is given by

$$\nabla E = \begin{bmatrix} \partial_{x_1} E & \partial_{x_2} E & \partial_{x_3} E & \cdots & \partial_{x_m} E & \partial_{y_1} E & \partial_{y_2} E & \partial_{y_3} E & \cdots & \partial_{y_m} E \end{bmatrix}^T. \quad (54)$$

Altogether, in our constrained optimization problem, we minimize the objective function in Eq. (39) subject to the length-preserving constraints in Eq. (3), the angle-preserving constraints in Eq. (8), and the no-overlap constraints in Eq. (23). For both the objective function and constraints, we further utilize their gradients as derived in Eq. (7), Eq. (21), Eq. (38), and Eq. (54) in the numerical optimization process.

2.3. Overlap correction

As mentioned previously, while the no-overlap constraint will attempt to prevent the occurrence of overlaps, it may overconstrain the problem. In other words, in some situations, it may happen that the planar embedding result is already overlap-free but the no-overlap constraint value is still non-zero. This may affect the computational efficiency of our optimization procedure as we may need to execute a large number of iterations or even need to wait until reaching some prescribed maximum number of iterations. Therefore, one strategy that we propose is that we can consider including or excluding the no-overlap constraint in our actual optimization procedure in an alternating manner. To achieve this, we need some extra procedures to detect and correct the overlaps in the intermediate embedding results. A correction scheme is developed as follows.

Between every iteration of each round of optimization run (with the no-overlap constraint included or excluded), we add a new process to remove

any overlaps in the current configuration. First, we will detect all overlaps O_n in the configuration. Note that each overlap O_n will involve exactly two rod segments, which are associated with exactly four points. We denote them as $\{P_{n_1}, P_{n_2}, P_{n_3}, P_{n_4}\}$. After getting this information, we use the Dijkstra algorithm to find the shortest path in the graph of the rod-based structure that will contain the four points. Also, we use the overlap point O_n as the center and create a circle with radius $r_n = \max\{\|O_n - P_{n_i}\|, i = 1, 2, 3, 4\}$. With the circle we just generated, we can consider all rod segments for which the rod midpoints are inside or lying on the circle. Then, we keep every point on the computed shortest path unchanged except the points P_{n_2} and P_{n_3} . Specifically, we allow each of those two points to shift along two circles with the center P_{n_1} and P_{n_4} and radii $\|P_{n_2} - P_{n_1}\|$ and $\|P_{n_3} - P_{n_4}\|$. We find two possible points that result in no overlaps inside the circle and in the path. In other words, we keep some key rod lengths unchanged while allowing the points to move the plane within a limited path in order to resolve the overlaps. Among all possible choices, we choose the point that gives the smallest length error with the vertex next to it in the path. If we cannot find any point that gives no overlaps, we will sacrifice some more length constraints and further consider two angle bisectors constructed by P_{n_2}, O_n and P_{n_3}, O_n respectively. We then find the possible points and choose the best one similarly as above.

Moreover, since resolving each overlap involves the four associated vertices, if multiple overlap points O_n are close to each other, a single step described above may only be able to resolve some overlaps but not all of them. Therefore, in practice, we repeat this approach at most 10 times before going into the next iteration of the optimization problem. Also, to prevent this process from

increasing the amount of overlaps, if the amount of overlaps increases after an iteration of this process, we will break the correction process and directly move to the next optimization iteration. The overlap correction algorithm is summarized in Algorithm 1.

Algorithm 1: Overlap correction

Data: A planar embedding $f : \mathcal{S} \rightarrow \mathbb{R}^2$

Result: A non-overlap transformation $T : \mathbb{R}^2 \rightarrow \mathbb{R}^2$

- 1 Detect all overlaps in the current configuration, and let $N_{overlap}$ be the number of overlaps;
- 2 Set $N_{iter} = 0$;
- 3 **while** $N_{overlap} > 0$ and $N_{iter} < 10$ **do**
- 4 **for** $i = 1, 2, \dots, N_{overlap}$ **do**
- 5 Locate the four vertices that correspond to the i -th overlap;
- 6 Construct a circle with radius equal to the maximum length from the overlap to the 4 points;
- 7 Locate all other points from the planar embedding that lie on or inside the circle;
- 8 Construct two circles using the first and the fourth point as centers, with radii being the length between the second and the first point, and the length between the third and the fourth point, respectively;
- 9 Shift the second and the third point along the two circles and find the optimal location that achieves the lowest length error and yields no overlap;
- 10 **if** *Cannot find any point satisfying our desired result* **then**
- 11 Consider the angle bisectors constructed by the second point and the overlap point, and the third point and the overlap point;
- 12 Allow the second and third points to shift on the angle bisectors again;
- 13 Update $N_{overlap}$ by the number of overlaps in the new configuration;
- 14 Set $N_{iter} = N_{iter} + 1$;

2.4. Summary

After describing our initial embedding method, shape optimization formulation, and overlap correction procedure, we are now ready to formulate our overall framework for the low-distortion planar embedding of rod-based structures.

Specifically, given a 3D rod-based structure, we first apply the initial embedding method to obtain a 2D representation. We then solved our proposed constrained optimization problem to update the vertex positions on the plane for reducing the geometric distortion while preserving bijectivity in an iterative manner. In particular, for the consideration of computational efficiency, we first check and see whether the current configuration contains overlap. If it does not contain any overlaps, then at the current step we only solve the constrained optimization problem with the no-overlap constraint in Eq. (23) skipped, so that we can focus on the reduction of the geometric distortion at this step without being overconstrained by the no-overlap constraint. Otherwise, we first apply the overlap correction scheme in Algorithm 1 and then run the full constrained optimization procedure with the no-overlap constraints, with the goal of handling both the geometric distortion and bijectivity issue at this step. The above procedure is repeated until the prescribed requirements on both the geometric distortion and bijectivity are satisfied. In practice, the convergence can be determined by some prescribed threshold on the length and angle errors E_{length} , E_{angle} and maximum number of iterations. The proposed algorithm is summarized in Algorithm 2.

Algorithm 2: Proposed framework for low-distortion planar embedding of rod-based structures

Data: A 3D rod-based structure $\mathcal{S} = (\mathcal{V}, \mathcal{E})$.

Result: A low-distortion planar embedding $f : \mathcal{S} \rightarrow \mathcal{P}$.

- 1 Compute an initial embedding $f_0 : \mathcal{S} \rightarrow \mathcal{P}_0$;
- 2 Compute the length and angle quantities;
- 3 Compute the length and angle errors $E_{\text{length}}, E_{\text{angle}}$;
- 4 Detect all overlaps in the current configuration, and let N_{overlap} be the number of overlaps;
- 5 Set $N_{\text{iter}} = 0$;
- 6 **while** ($E_{\text{length}} > 10^{-4}$ or $E_{\text{angle}} > 10^{-4}$ or $N_{\text{overlap}} > 0$) and $N_{\text{iter}} \leq 10$ **do**
- 7 **if** $N_{\text{iter}} = 0$ **then**
- 8 Solve the full constrained optimization problem with the length, angle, and no-overlap constraints in Eq. (3), Eq. (8), and Eq. (23);
- 9 **if** $N_{\text{overlap}} = 0$ **then**
- 10 Solve the constrained optimization problem without the no-overlap constraint in Eq. (23);
- 11 **else**
- 12 Apply the overlap correction algorithm (Algorithm 1);
- 13 Solve the full constrained optimization problem with the length, angle, and no-overlap constraints in Eq. (3), Eq. (8), and Eq. (23);
- 14 **if** $N_{\text{overlap}} > 0$ **then**
- 15 Apply the overlap correction algorithm (Algorithm 1);
- 16 Denote the final vertex positions as p_{opt} and the shape optimization mapping as $g : \mathcal{P}_0 \rightarrow \mathcal{P}$. The final embedding f is given by $f = g \circ f_0$, and we have $f(v_i) = (p_{\text{opt}})_i$;

3. Experimental results

The proposed algorithms are implemented using MATLAB R2024b. All experiments are performed on a MacBook Pro with an Apple M4 Pro chip and 24 GB memory. The optimization is solved using the interior-point method in MATLAB.

We first quantify the geometric distortion of the planar embedding produced by our method. Here, the *average length error* is defined as the mean of the absolute length error of each rod. The *angle error* is defined as the mean of the absolute error of each angle that connects to more than two rods. Also, the number of overlaps in the planar embedding result is checked using the InterX function [15] in MATLAB.

More specifically, for the illustration example shown in Fig. 1, we measure the error in length and angle for the planar embedding result and visualize the errors in Fig. 3. Here, the rod segment length error is defined as the difference between the original rod segment length in 3D and that in the resulting 2D representation. As shown in Fig. 3(a), the length error is of the order 10^{-4} for most rod segments, suggesting that the proposed method is highly length-preserving. We also assess the angle error at the joints of the rod-based structure, defined as the difference between the original angles in 3D and the corresponding angles in the final planar representation. As shown in Fig. 3(b), the angle error is very close to 0 at all joints. This shows that the proposed method is highly accurate and is capable of preserving the required geometrical properties. Besides, one can also calculate the number of overlaps between all pairs of rod segments. The result shows that the planar embedding result does not contain any overlaps. In other words, the

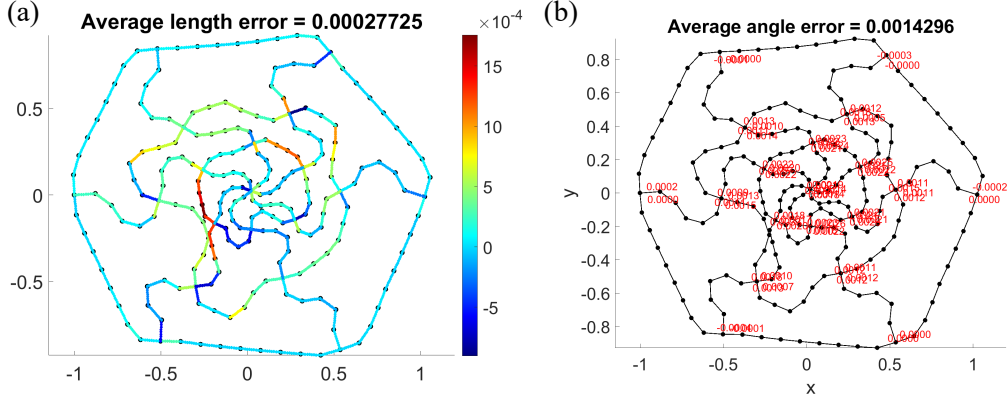


Figure 3: **Quantification of the geometric distortion of the example shown in Fig. 1.** (a) The planar embedding result, with every rod segment color-coded with the length error. (b) The angle error at each intersection point of the rods.

bijectivity of the rod-based structure is well-preserved.

Besides the above example, Fig. 4 (top row) shows three other examples of rod-based structures with different geometries and curvature properties. From the corresponding planar embedding results (bottom row), it can be observed that the rod segment lengths, angles at the joints, and the bijectivity are all well-preserved.

After demonstrating the effectiveness of the proposed method on handling the above examples, we consider some more complex examples. Specifically, in Fig. 5(a) we consider a rod-based structure representing a cloth surface. In Fig. 5(b), we further consider a rod-based structure representing a human face. For both examples, our method is capable of producing a low-distortion planar embedding without overlaps.

For a more quantitative analysis of the above experiments, Table 1 shows the performance of our method (in terms of length error, angle error, and overlap number) on different examples. In all examples, we can see that

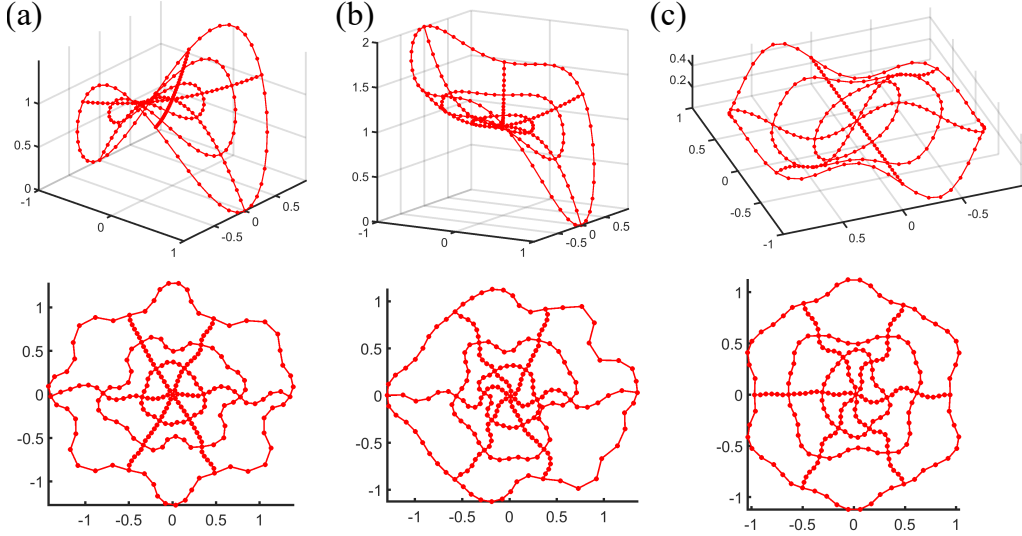


Figure 4: **Three examples of rod-based structures with different geometries (top) and the corresponding planar embeddings (bottom).** (a) A doubly curved rod-based structure. (b) A rod-based structure with a more prominent height variation. (c) A rod-based structure with multiple peaks.

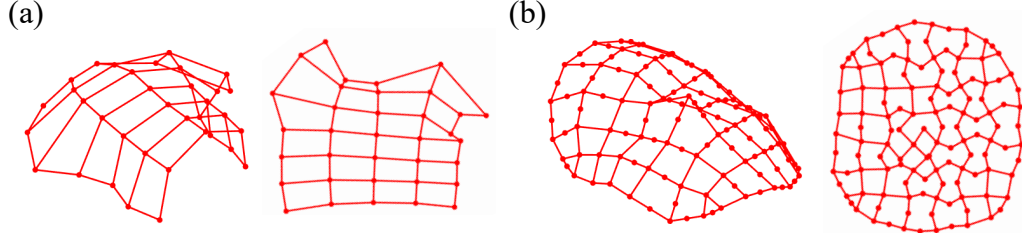


Figure 5: **Two examples of rod-based structures representing different surfaces and the corresponding planar embedding.** (a) The *Cloth* surface model. (b) The *Sophie* surface model.

the length and angle errors are very small, indicating that the embeddings exhibit low geometric distortion. We remark that the angle error is relatively large for the two surface examples (Fig. 5(a) and Fig. 5(b)) because of the large number of joints between short rod segments. Specifically, the short rod segments unavoidably pose some limitations on the movement of the vertices

Example	Length error (Mean/SD)	Angle error (Mean/SD)	Overlap number
Fig. 1	$2.8 \times 10^{-4} / 3.2 \times 10^{-4}$	$1.4 \times 10^{-3} / 8.8 \times 10^{-4}$	0
Fig. 4(a)	$8.1 \times 10^{-3} / 1.8 \times 10^{-2}$	$3.9 \times 10^{-4} / 3.6 \times 10^{-4}$	0
Fig. 4(b)	$6.2 \times 10^{-4} / 1.1 \times 10^{-3}$	$7.1 \times 10^{-4} / 9.5 \times 10^{-4}$	0
Fig. 4(c)	$1.4 \times 10^{-4} / 3.5 \times 10^{-4}$	$9.7 \times 10^{-4} / 1.7 \times 10^{-3}$	0
Fig. 5(a)	$7.4 \times 10^{-2} / 1.3 \times 10^{-1}$	$7.3 \times 10^{-2} / 1.6 \times 10^{-1}$	0
Fig. 5(b)	$4.6 \times 10^{-5} / 8.4 \times 10^{-5}$	$1.5 \times 10^{-1} / 2.0 \times 10^{-1}$	0

Table 1: Performance of our method on different rod-based structures.

on the plane throughout the optimization process, thereby causing a relatively large angle error when compared to the other examples. Besides, the number of overlaps is 0 for all examples, confirming the bijectivity of the embeddings.

4. Extension to hybrid structures

In some cases, the structure may consist not only of one-dimensional rods but also of some surface regions. Besides preserving the geometry of the rods, one may also want to preserve the geometry of those surface regions in the embedding result as much as possible. Here, we consider extending our approach to handle the embedding of such hybrid structures.

Specifically, we first use additional rods to form a local mesh that fills the surface regions. Then, we run our proposed algorithm with the geometry of these additional rods also considered. Because of the conditions required in our algorithm, the lengths and angles of these additional rods will also be preserved as much as possible. In other words, the optimization result will be a low-distortion planar embedding of the hybrid structure, with the isometric distortion (in both lengths and angles) reduced as much as possible.

To examine the performance of this approach, Fig. 6 shows three examples of hybrid structures with different geometries. First, in Fig. 6(a) we consider

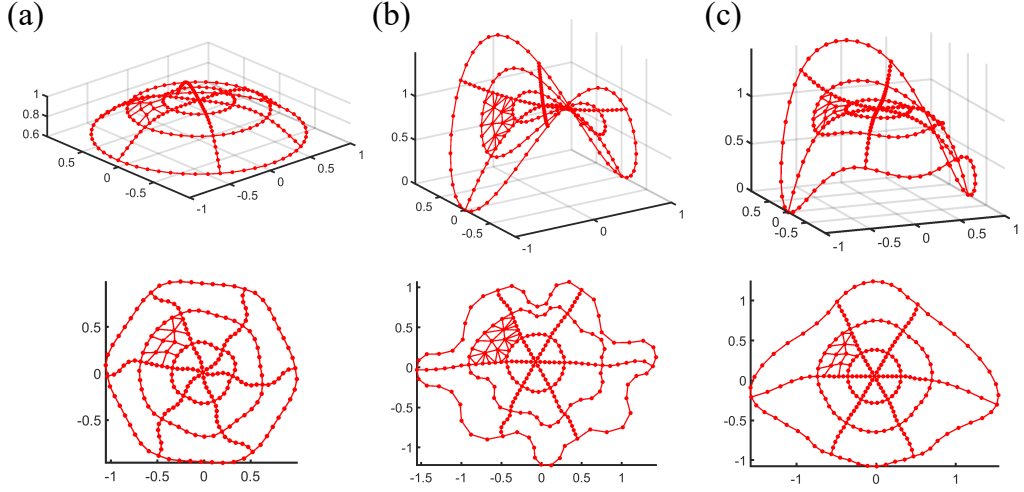


Figure 6: **Three examples of hybrid structures with different geometries (top) and the corresponding planar embeddings (bottom).** (a) A dome-shaped hybrid structure. (b) A doubly curved hybrid structure. (c) a hybrid structure with multiple peaks.

a positively curved structure formed primarily by rods, with an additional surface region to be preserved. We then consider a doubly curved structure with an additional surface region as shown in Fig. 6(b). Finally, we consider another curved structure with greater asymmetry and fluctuations in shape, again with an additional surface region to be preserved. For all these hybrid structure examples, our proposed algorithm is capable of producing the desired planar embeddings.

Table 2 shows the detailed performance analyses of our method on different hybrid structures. It can be observed that while the inclusion of the surface regions makes the optimization problem overconstrained, both the length and angle errors remain very small. Also, the number of overlaps is 0 in all examples. This demonstrates the effectiveness and generalizability of our proposed framework for handling a wider class of rod-based structures.

Example	Length error (Mean/SD)	Angle error (Mean/SD)	Overlap number
Fig. 6(a)	$2.6 \times 10^{-3} / 6.5 \times 10^{-3}$	$4.2 \times 10^{-3} / 1.2 \times 10^{-2}$	0
Fig. 6(b)	$1.7 \times 10^{-2} / 3.8 \times 10^{-2}$	$3.8 \times 10^{-3} / 1.2 \times 10^{-2}$	0
Fig. 6(c)	$4.2 \times 10^{-3} / 1.1 \times 10^{-2}$	$5.6 \times 10^{-3} / 1.8 \times 10^{-2}$	0

Table 2: Performance of our method on different hybrid structures.

5. 2D-to-3D morphing process of the planar embeddings

As discussed earlier in this work, the low-distortion planar embeddings of rod-based structures produced by our proposed algorithm can be utilized for various applications. In particular, the planar embeddings can be regarded as simplified 2D representations of the original 3D rod-based structures, which facilitate their manufacturing and storage. It is therefore natural to ask whether we can restore the 3D structures from the planar embedding results.

Here, we simulate the 2D-to-3D morphing process using the deployment simulation approach in [14], which considers a spring energy model to simulate the deployment process. In particular, here we treat all rods as springs and apply a pulling force on a selected group of vertices iteratively, starting from the 2D planar configuration of the structure. The rest of the structure is then also deployed following the spring energy minimization process, constrained by the displacement of the selected pulling points. The deployment ends when the selected pulling points reach the final position of the 3D rod-based structure.

To demonstrate this idea, we consider the 2D-to-3D deployment process of the rod-based example in Fig. 1. In Fig. 7, we show snapshots of the deployment of the structure from the planar embedding state produced by our algorithm to the final 3D configuration. Here, we select only the rod intersection points (in black) as the pulling points and apply the above-

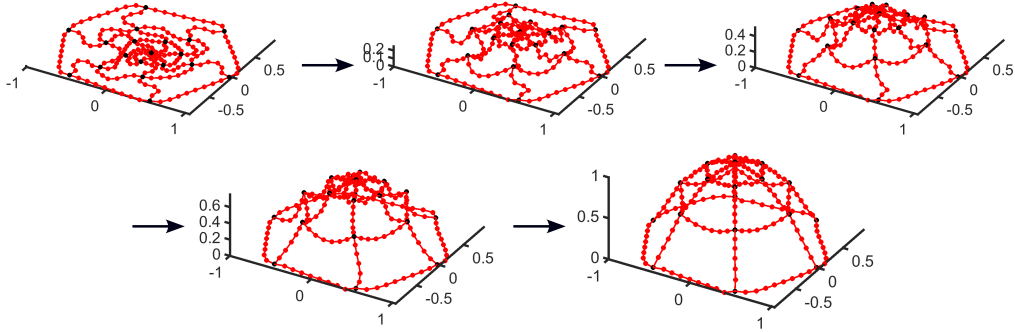


Figure 7: **Simulated deployment process of a rod-based structure from the planar configuration obtained by our low-distortion embedding method (top left) to the final 3D configuration (bottom right).** The black nodes indicate the pulling points.

mentioned spring energy model to simulate the deployment over time. It can be observed that the structure effectively morphs from the 2D state into the final 3D state, which matches the shape of the original 3D rod-based structure very well. From this experiment, we can see that the planar embeddings produced by our proposed algorithm can be effectively used in practical applications.

6. Conclusion

In this work, we have developed a novel method for the planar embedding of 3D structures composed of rod segments. Specifically, our method preserves the rod segment length and the intersection angles between the rods, thereby maintaining the key geometrical properties of the rod-based structures. Also, our method effectively prevents overlaps between rod segments in the planar embedding, thereby facilitating the practical fabrication and use of the planar representations. We have demonstrated the applicability of the method to

a wide range of rod-based structures with different shapes. We have also demonstrated the feasibility of extending the formulation to hybrid structures. Using a simple mechanical model, we have further shown that the deployment from the 2D embedding to the desired 3D shape can be easily achieved. Altogether, our work paves a new way to the representation and simplification of rod-based structures.

In our future work, we plan to extend our approach and consider a broader range of rod-based structures with spatially varying elasticity conditions, allowing some parts of the structure to become more flexible and exhibit greater geometric distortions. To achieve this, one possible approach is to turn the equality constraints on lengths and angles in our current optimization problem into inequality constraints, imposing different bounds on different edges and angles to control their distortions.

Declaration of Competing Interest

The author declares no conflict of interest.

Acknowledgements

We thank Dr. Mahmoud Shaqfa (ETH Zurich) for useful discussions.

References

- [1] B. Wang, H. Wang, E. Schling, H. Pottmann, Rectifying strip patterns, ACM Transactions on Graphics 42 (1) (2023) 1–18.

- [2] A. Sydney Gladman, E. A. Matsumoto, R. G. Nuzzo, L. Mahadevan, J. A. Lewis, Biomimetic 4D printing, *Nature Materials* 15 (4) (2016) 413–418.
- [3] G. Risso, M. Sakovsky, P. Ermanni, A highly multi-stable meta-structure via anisotropy for large and reversible shape transformation, *Advanced Science* 9 (26) (2022) 2202740.
- [4] D. Liu, D. Pellis, Y.-C. Chiang, F. Rist, J. Wallner, H. Pottmann, Deployable strip structures, *ACM Transactions on Graphics* 42 (4) (2023) 1–16.
- [5] X. Wang, Y. Mei, M. Y. Wang, Level-set method for design of multi-phase elastic and thermoelastic materials, *International Journal of Mechanics and Materials in Design* 1 (3) (2004) 213–239.
- [6] C. Baek, A. O. Sageman-Furnas, M. K. Jawed, P. M. Reis, Form finding in elastic gridshells, *Proceedings of the National Academy of Sciences* 115 (1) (2018) 75–80.
- [7] L. Qin, W. Huang, Y. Du, L. Zheng, M. K. Jawed, Genetic algorithm-based inverse design of elastic gridshells, *Structural and Multidisciplinary Optimization* 62 (2020) 2691–2707.
- [8] R. Guseinov, C. McMahan, J. Pérez, C. Daraio, B. Bickel, Programming temporal morphing of self-actuated shells, *Nature Communications* 11 (1) (2020) 237.
- [9] A. Martín-Pastor, F. González-Quintial, Surface discretisation with rectifying strips on geodesics, *Nexus Network Journal* 23 (3) (2021) 565–582.

- [10] J. Panetta, F. Isvoranu, T. Chen, E. Siéfert, B. Roman, M. Pauly, Computational inverse design of surface-based inflatables, *ACM Transactions on Graphics* 40 (4) (2021) 1–14.
- [11] Y. Ren, J. Panetta, S. Suzuki, U. Kusupati, F. Isvoranu, M. Pauly, Computational homogenization for inverse design of surface-based inflatables, *ACM Transactions on Graphics* 43 (4) (2024) 1–18.
- [12] E. Schling, H. Wang, S. Hoyer, H. Pottmann, Designing asymptotic geodesic hybrid gridshells, *Computer-Aided Design* 152 (2022) 103378.
- [13] W. T. Tutte, How to draw a graph, *Proceedings of the London Mathematical Society* 3 (1) (1963) 743–767.
- [14] G. P. T. Choi, L. H. Dudte, L. Mahadevan, Programming shape using kirigami tessellations, *Nature Materials* 18 (9) (2019) 999–1004.
- [15] NS, Curve intersections, MATLAB Central File Exchange, <https://www.mathworks.com/matlabcentral/fileexchange/22441-curve-intersections>, accessed on June 26, 2025 (2010).